Structural Analysis of MBE Grown InGaAsSb Films

Rosemary Wynnychenko
Department of Physics, University of California, Santa Barbara, California 93106, USA and
Department of Physics, Wellesley College, Wellesley, Massachusetts 02481, USA

Faculty Advisor: Chris Palmstrøm
Department of Materials and Department of Electrical and Computer Engineering,
University of California, Santa Barbara, Santa Barbara, CA 93106, USA

Graduate Advisors: Yu Wu and Teun van Schijndel
Department of Electrical and Computer Engineering,
University of California, Santa Barbara, Santa Barbara, CA 93106, USA
(Dated: December 1, 2025)

Thermoelectric devices utilize a temperature gradient to generate a voltage and thus have the potential to convert waste heat to usable electricity. Efficient thermoelectrics require materials with high electrical conductivity and low thermal conductivity. However, electrical and thermal conductivity are typically inversely related, limiting the efficiency of thermoelectric devices. One method of improving device efficiency is using entropy-driven thermoelectrics, whose structure leads to high electrical conductivity with minimal increase of thermal conductivity. InGaAsSb is a quaternary semiconductor alloy that has potential for use in thermoelectric devices and has other possible applications for infrared devices and thermophotovoltaics. In this work, we study the growth of InGaAsSb as a potential thermoelectric material candidate. We investigate how growth conditions impact the lattice constant of $In_{0.5}Ga_{0.5}As_ySb_{1-y}$ with the goal of understanding how to grow $In_{0.5}Ga_{0.5}As_ySb_{1-y}$ lattice-matched to GaSb, a lattice constant that requires growing inside the miscibility gap. We achieve a lattice constant of 6.12±0.02 Å, which is only a 0.34% mismatch from the lattice constant of GaSb (6.095 Å). This indicates that growth within the miscibility gap has been achieved through using Molecular Beam Epitaxy (MBE). We have found that low temperature growth (430 °C) allows us to achieve lattice constants closer to that of GaSb. However, at higher temperature growth, there is a rapid change in lattice constant near values close to the lattice constant of GaSb.

I. INTRODUCTION

Over two thirds of used energy is lost as wasted heat [1]. As a result, thermoelectrics, which are devices that use a temperature gradient to extract a voltage, have the potential to assist in reducing energy waste by using this waste heat to generate more power. Due to a lack of materials which are well suited for thermoelectrics, current thermoelectrics are not sufficiently efficient.

The maximum efficiency of a thermoelectric device depends on the figure of merit, zT, of the device materials [2]. The material figure of merit is given by

$$zT = \frac{\sigma S^2 T}{\kappa_L + \kappa_e} \tag{1}$$

where σ is the electrical conductivity, S is the Seebeck coefficient, κ_L is the lattice thermal conductivity and κ_e is the electrical thermal conductivity [3]. The Seebeck coefficient and σ depend on the charge carriers mobility, concentration, and effective mass while κ_L depends on the materials phonon properties [3]. Unfortunately, thermal and electrical conductivity are positively correlated, presenting challenges to the goal of increasing zT [3]. Thus, designing material structures that increase electrical conductivity without increasing thermal conductivity is needed in order to achieve more efficient thermoelectric devices with the potential to better convert waste heat to usable energy.

InGaAsAb is a semiconductor compound with a widely tunable band gap ranging from 0.28-0.73 eV [4]. As a result, it has potential applications such as use in thermophotovoltaics and infrared detectors, imaging, LEDs and lasers. This paper focuses on utilizing InGaAsSb for thermoelectric devices. A diagram of the goal device component is shown in Figure 1. This structure works to increase electrical conductivity while minimally increasing thermal conductivity through creating an entropy driven structure.

The use of both InAsSb and InGaAsSb layers works to increase electrical conductivity by utilizing the principle of maximizing entropy. When InAsSb and InGaAsSb are both lattice matched to GaSb, InGaAsSb has a higher bandgap energy than InAsSb [5]. As a result of its narrower bandgap, InAsSb has a lower density of states and higher carrier mobility. This is because a narrower bandgap leads to stronger interband coupling between the valence band and the conduction band in the semiconductor. A sharper conduction band curvature implies a lower effective mass as the effective mass is inversely related to the conduction band curvature [6]. This means there's a lower density of states and higher electron mobility [6]. Comparatively, InGaAsSb will have a higher density of states due to the opposite causes. By defini-

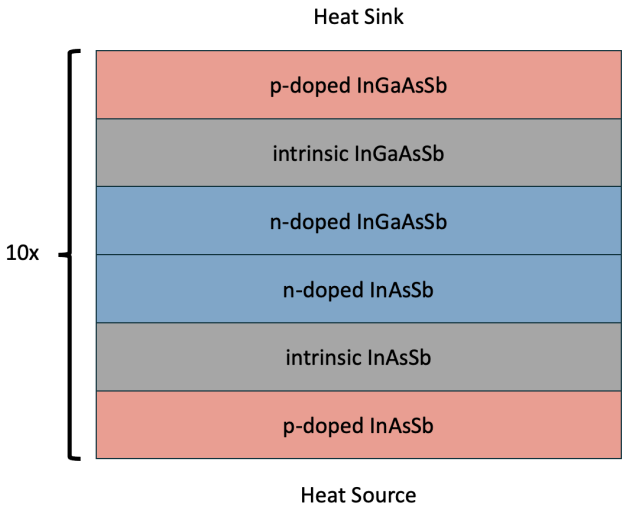

FIG. 1. Diagram of the thermoelectric device composed of InAsSb and InGaAsSb sections, both of which are lattice matched to GaSb. Each layer is 300 nm thick.

tion, a material with a lower density of states has less available states at a given energy level while a material with a higher density of states has more available states at a given energy level. When the system is in equilibrium, the system will move towards a state of higher entropy. Configurational entropy is maximized when the electrons are in higher density of state regions. As a result, the InAsSb/InGaAsSb structure will increase the electrical conductivity by providing entropy driven incentives for electrons to flow from InAsSb to InGaAsSb.

Furthermore, as shown in Figure 1, each InAsSb and InGaAsSb layer contains p-doped, intrinsic and n-doped layers. The n-doped layer will have a smaller effective mass as electrons are the carriers. As the density of states is proportional to the effective mass, the n-doped layer will thus have a lower density of states [7]. However, in the p-doped regions the carriers are holes with a larger effective mass and so there is a higher density of states. The undoped region will act as an entropy filter or buffer so only higher energy carriers can pass enhancing the average carrier energy. This serves to maximize electrical conductivity, which depends on the carrier energy, without increasing the thermal conductivity.

Based on simulations provided by our collaborators, $In_{0.5}Ga_{0.5}As_ySb_{1-y}$ lattice matched to GaSb has the potential to improve the overall efficiency of the goal thermoelectric devices. Thus, this paper studies the growth of $In_{0.5}Ga_{0.5}As_ySb_{1-y}$ lattice matched to GaSb. X-Ray Diffraction (XRD) is used to measure the lattice constant of the InGaAsSb samples.

$In_{0.5}Ga_{0.5}As_ySb_{1-y}$ lattice matched to GaSb is particularly difficult to grow because of the existence of a miscibility gap, meaning that certain compositions of $In_{0.5}Ga_{0.5}As_ySb_{1-y}$ typically phase separate during growth.

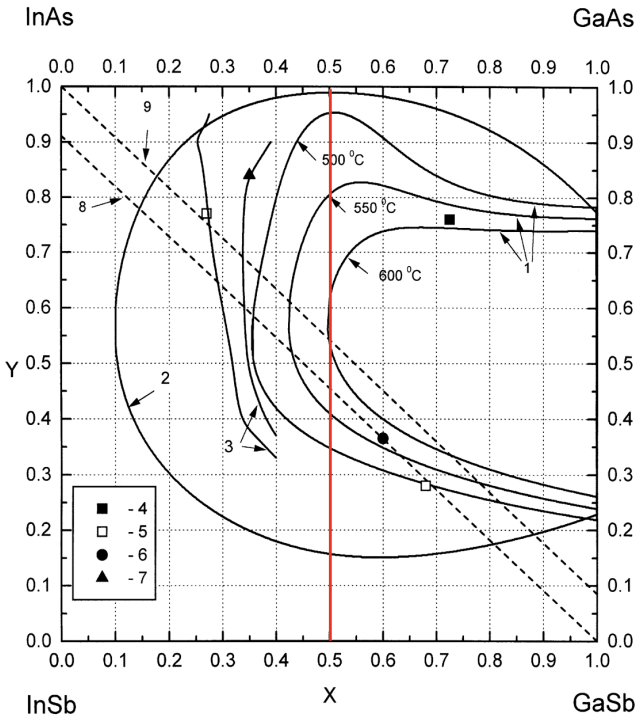

FIG. 2. Theoretical curves predicting the miscibility gap at different temperatures [8]. The red line (added) demonstrates the possible compositions of $In_{0.5}Ga_{0.5}As_ySb_{1-y}$. At the temperatures used for growing InGaAsSb during Molecular Beam Epitaxy, growth always occurs in the miscibility gap.

Previous experimental work has confirmed this phenomena. Müller and Richards combined different semiconductor compounds via flash evaporation and found that at 50% InAs in InAs-GaSb or 50% GaAs in GaAs-InSb mixtures, there is a wide composition range in the resulting material indicating the existence of a miscibility gap [9]. Sabardeil et al varied Ga composition in GaAsInSb alloys latticed matched to GaSb and found that for 50% Ga there was poor crystal quality implying a miscibility gap [10]. Figure 2 shows theoretical calculations for the miscibility gap in InGaAsSb. Growing $In_{0.5}Ga_{0.5}As_ySb_{1-y}$ lattice matched to GaSb via Molecular Beam Epitaxy thus requires growing in the miscibility gap.

II. METHODS

A. Sample Growth

Samples for this paper were grown in a VG V80H Molecular Beam Epitaxy (MBE) system. During MBE, a sample is placed in an ultra high vacuum chamber and atoms from cells containing the elements for deposition are directed at the sample. Under the right conditions, an epitaxial thin film can be grown on the substrate. GaSb

(100) substrates were used in this study. Each substrate first had a GaSb or InAsSb layer deposited. Then InGaAsSb layers were grown. Generally, three layers of varying compositions were grown on each sample.

The substrate growth temperatures for films grown in this study ranged between 400°C and 500°C. Phase separation was observed at 400°C so the vast majority of samples were grown at temperatures ranging between 420°C and 500°C. The substrate temperature was measured by a pyrometer which determines the sample temperature by measuring the emitted radiation. The pyrometer is calibrated for each sample growth by finding the pyrometer reading at which the oxidized layer on the substrate desorbs. This value is known from the literature and is used to calibrate the pyrometer for each growth. The moment at which the oxidized layer desords is determined by changes in the reflection high-energy electron diffraction (RHEED) pattern from the sample. During this process, a steady flux of Sb_2 is directed at the sample to prevent Antimony from desorbing.

The composition of the deposited films was determined by the effusion cell parameters. Thermal effusion cells are used for Indium and Gallium meaning the flux from these cells is set by the cell temperature. The flux from these cells is determined by using oscillations in reflection high-energy electron diffraction (RHEED) patterns from the sample. The effusion cells for Indium and Gallium were set such that their fluxes were equal so all films are $In_{0.5}Ga_{0.5}As_ySb_{1-y}$. The flux from the Antimony and Arsenic cells is controlled by the valve position on a valved cracker cell. A flux gauge was used to determine the Antimony (Arsenic) flux at different valve positions, allowing for the conversion of a valve position to a flux. By comparing the flux of Antimony and Arsenic, the relative composition of Antimony and Arsenic is predicted.

B. X-Ray Diffraction (XRD)

A Rigaku HyPix 2000 X-ray diffractometer was used to analyze the structural properties of each InGaAsSb sample. During XRD, a beam of x-rays is directed at a sample. A detector is used to measure the intensity of the diffraction pattern as a function of angle. The angle of the X-ray source beam relative to the sample, ω, and angle of the detector relative to the source beam 2θ can be varied while the intensity of the scattered X-rays is measured. If the scan the angle ω is kept to half of the 2θ angle, the scan is referred to as a $2\theta/\omega$ scan [11]. A diagram of such a setup is shown in Figure 3.

As shown in Figure 4, X-rays can interact with and scatter off of the top layer of atoms on the sample surface, the second layer of atoms from the surface and so on. Peaks in the intensity as a function of 2θ occur when there is constructive interference between the X-ray beams scattered off of different layers in the sample. Constructive interference occurs when the path length difference, $2d\sin(\theta_B)$ where d is the lattice constant and

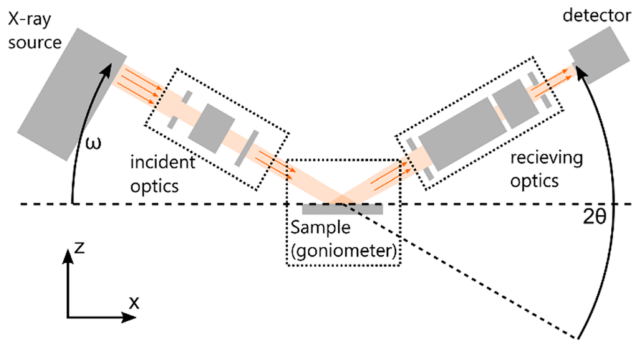

FIG. 3. Diagram of an X-ray diffractometer [11].

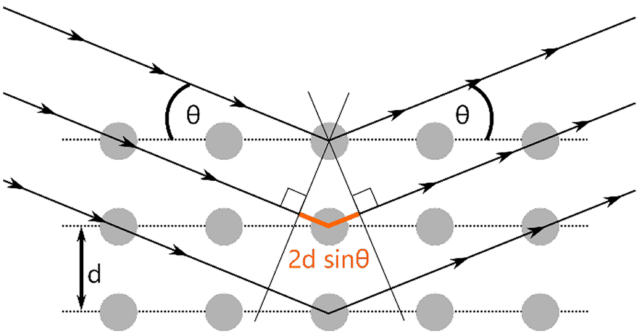

FIG. 4. A diagram demonstrating the derivation of Bragg's law [11].

θ_B is half of the 2θ angle, is equal to an integer number of wavelengths. This is demonstrated in Figure 4. Thus, Bragg's law follows:

$$n\lambda = 2d\sin(\theta_B) \tag{2}$$

where n is the order of the diffraction and λ is the x-ray wavelength.

III. RESULTS AND DISCUSSION

X-ray diffraction data was taken for multiple samples. Using Bragg's law, the lattice constant corresponding to each individual peak is found. Example XRD data is shown in Figure 5. Each lattice constant was then correlated with its corresponding sample composition and growth temperature. A table of samples measured and their corresponding XRD peaks and lattice constants is shown in the Appendix. Figure 6 was then created using the known growth properties and corresponding lattice constants in order to understand how the lattice constant varies as a function of substrate temperature and composition. Using this data, a lattice constant of 6.12±0.02 Å was achieved using a substrate growth temperature of 430°C and a composition of $In_{0.5}Ga_{0.5}As_{0.122}Sb_{0.878}$, as

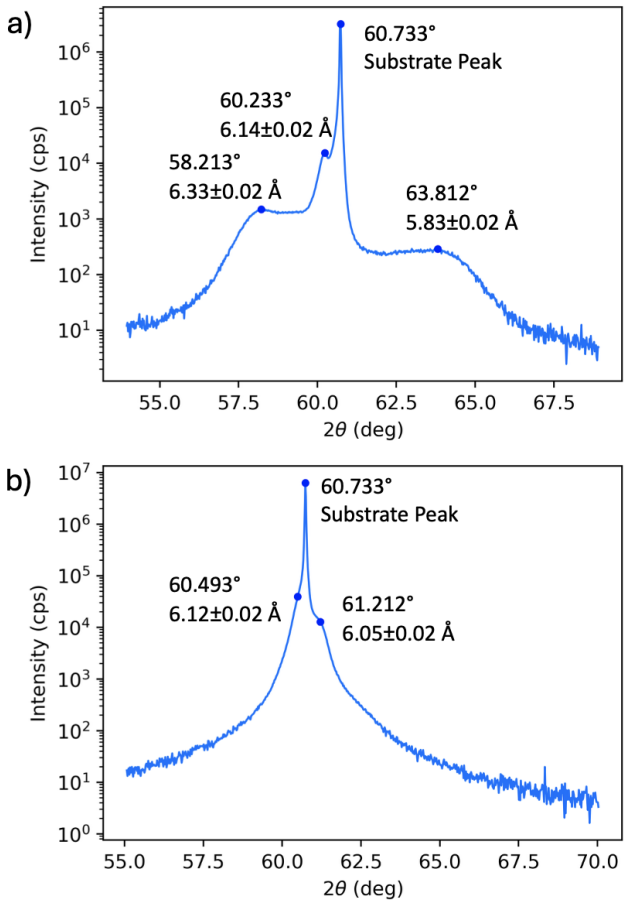

FIG. 5. Example XRD data for two different samples are shown. Each sample is composed of three separate layers of $In_{0.5}Ga_{0.5}As_ySb_{1-y}$ of varying compositions grown on GaSb. For both samples the substrate peak, corresponding to an angle of 60.733°, is clear. In graph A, three other peaks corresponding to the three sample layers of differing compositions are visible. In graph B, the peaks are overlapping. Blue dots are used to denote the visible peak locations. Graph B only shows two sample peaks as opposed to the three we would expect. This is potentially because the third sample peak has so much overlap with the other peaks that it is not visible. The lattice constant corresponding to all visible peak angles is shown. Graph B also shows that a lattice constant of 6.12±0.02 Å has been achieved.

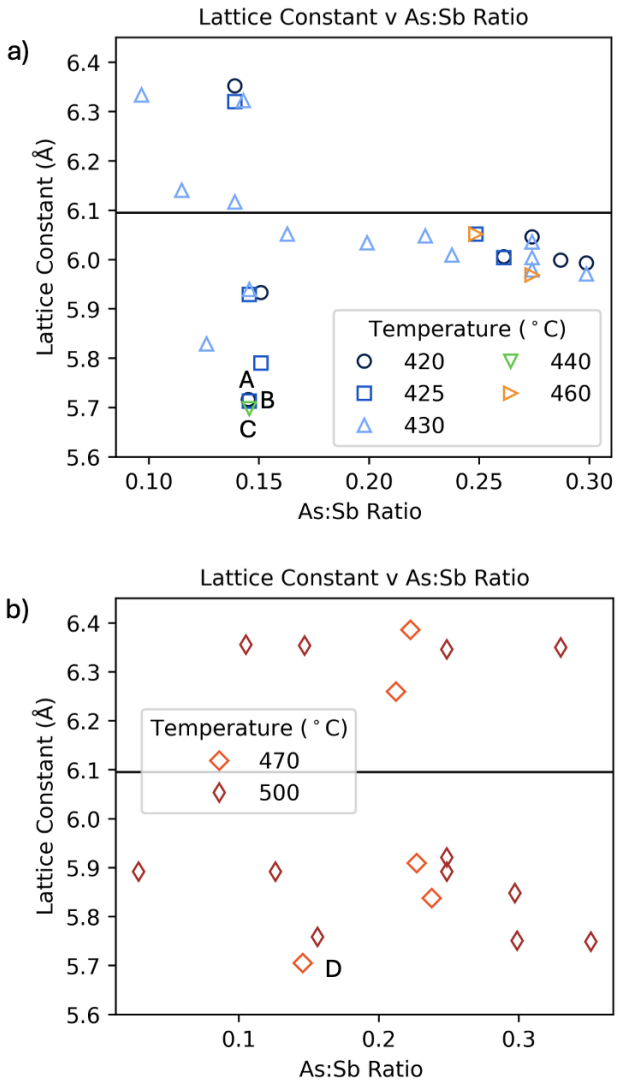

FIG. 6. Graphs showing the lattice constant as a function of the Arsenic to Antimony ratio for a variety of growth temperatures. Graph A shows low temperature growth (420°C, 425 °C, 430°C, 440°C, 460°C) while graph B shows higher temperature growth (470°C, 500°C).

shown in Figure 5. This lattice constant is within 0.34% of the lattice constant of GaSb (6.0955 Å).

A. InGaAsSb Film Composition Only Depends on the Arsenic Flux

The lattice constant (and thus composition) of the InGaAsSb thin films is independent of the Antimony flux, as shown in Figure 7a. Comparatively, Figures 7b and 7c shows that the lattice constant of InGaAsSb thin films is not independent of Arsenic Flux. These results reflect the fact that Arsenic sticks better to the surface of the sample at a given temperature. As a result, Antimony is more likely to desorb from the sample than Arsenic. Thus, the lattice constant and sample composition only depend on the Arsenic flux.

B. Low and High Substrate Temperature Growth

Data specific to low temperature growth is shown in Figure 6a. At low temperatures, a linear relationship between lattice constant and ratio of Arsenic to Antimony is tentatively observed. As the Arsenic to Antimony ratio increases, the lattice constant decreases reflecting the

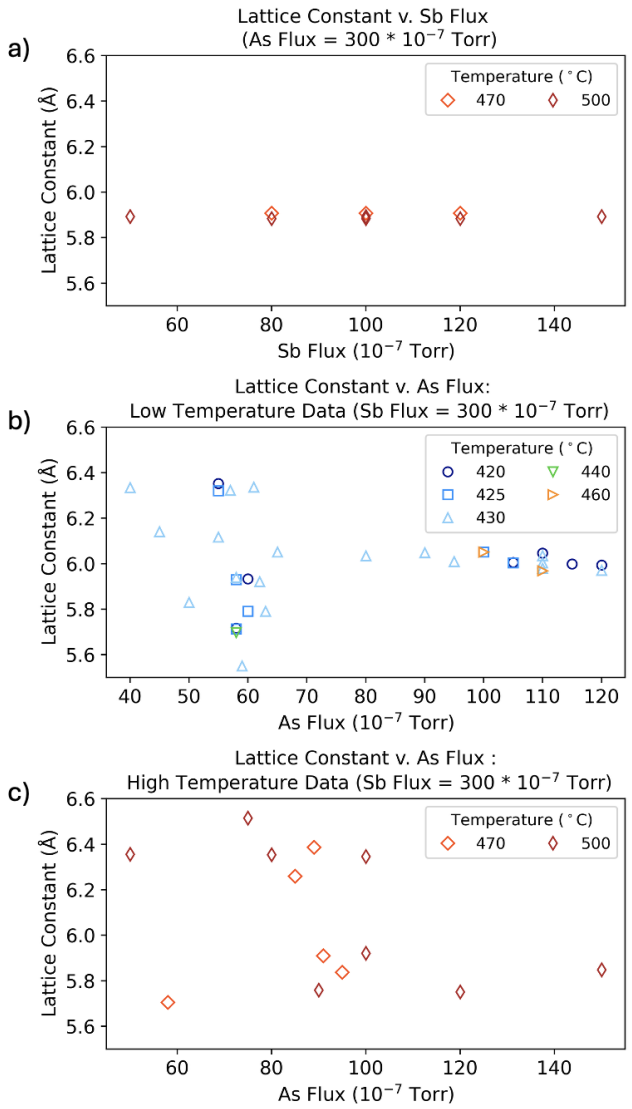

FIG. 7. Graph A shows the lattice constant as a function of Sb flux while As flux is held constant. Graphs B and C show the lattice constant as a function of As flux while Sb flux is constant.

fact that InGaAs has a smaller lattice constant than InGaSb. At higher temperatures (470°C, 500°C), there is a rapid increase in lattice constant at values near the lattice constant and values sufficiently close to the lattice constant of GaSb were not achieved. This suggests that a miscibility gap prevents growth of a lattice constant near 6.095 Å (the lattice constant of GaSb). At lower temperatures (Figure 6a), the miscibility gap is avoided and growth in the miscibility gap occurs as the atoms do not have sufficient energy to phase separate. However, at higher temperatures (Figure 6b), the atoms have sufficient energy to phase separate so a miscibility gap occurs.

The graphs in Figure 6 clearly contain numerous outliers. A few factors significantly impact the quality of the data. First, it is difficult to measure temperature in a ultra high vacuum chamber. The substrate growth temperature is regulated using a pyrometer which measures the radiation emitted from a sample to determine its temperature. Different sample holders can have different emissivity values meaning that samples grown with different sample holders may have been grown at different temperatures, even if the temperature given by the pyrometer is the same. Furthermore, the temperature scaling is recalibrated for each sample, meaning that even samples grown with the same block may have been grown with different temperatures even if the temperature is denoted as being the same. This is impactful as we observe a significant temperature dependence in the lattice constant. This would account for some of the variability in the data in Figure 6.

Second, not all points in the graphs in Figure 6 correspond to samples grown on the same substrate. Points labeled A, B, C in Figure 6a and point D in Figure 6b where grown on a GaSb substrate with an InAsSb layer first grown on top. All other samples were grown on a GaSb substrate. As different substrates will lead to a different nucleation process, it is not unexpected that the samples grown on InAsSb are outliers relative to the samples grown on GaSb. Furthermore, InAsSb and GaSb have different emissivity values affecting the pyrometer reading, leading to a likely differences in temperature between samples grown on GaSb and InAsSb even if we believe they're grown on the sample.

Third, the Arsenic to Antimony ratio is calculated based on the relative Arsenic and Antimony fluxes. The temperature of the Arsenic and Antimony crackers can be varied in order to change the respective fluxes. Throughout the course of this study we observed that the temperature of the Arsenic cracker needed to achieve equal Arsenic and Antimony fluxes increased. This indicates that the Arsenic crucible is running low in Arsenic. Thus, for some data points the actual Arsenic to Antimony ratio might be lower than expected (and indicated by the graph), adding further noise and uncertainty to our data points.

IV. CONCLUSION

This work studied the impact of growth parameters (substrate temperature and composition) on the lattice constant of $In_{0.5}Ga_{0.5}As_ySb_{1-y}$ with the goal of growing $In_{0.5}Ga_{0.5}As_ySb_{1-y}$ lattice matched to GaSb. We found that $In_{0.5}Ga_{0.5}As_{0.122}Sb_{0.878}$ grown at 430°C achieved a lattice constant within within 0.34% of the lattice constant of GaSb (6.0955 Å). Thus, growth within the miscibility gap has been achieved. In this study's investigative work, it was also found that at lower temperatures (430°C) a linear relationship between the lattice constant and the Arsenic to Antimony ratio was observed. However, at higher growth temperatures (470°C or above) a rapid increase in lattice constant at values near the lat-

tice constant was observed. Additionally, we found that the lattice constant and thus composition is independent of the Antimony flux, reflecting the fact that Antimony sticks better to the substrate. Maintaining consistent Arsenic flux and temperature readings is critical and limitations in our ability to do so led to a significant number of outlier points. Future investigation at low growth temperatures is needed to further optimize the lattice matching between $In_{0.5}Ga_{0.5}As_ySb_{1-y}$ and GaSb. Additionally, further exploration of higher growth temperatures is needed to better understand the pattern of rapid increase.

ACKNOWLEDGMENTS

I am very grateful for Professor Christopher Palmstrøm's support and enthusiasm throughout the REU program. I am also thankful for the help of You Wu and Teun van Schijndel without whom I would not have been able to learn so much about X-ray diffraction and molecular beam epitaxy. Additionally, I am grateful for the time Wilson Yanez took to teach me about ARPES and his enthusiasm for physics. I would also like to thank the entire Palmstrøm lab for being so welcoming. Finally, thank you to REU site director Professor Sathya Guruswamy for all her work supporting the REU program. This project would have not been possible without the generous support of all those involved. This work is supported by NSF REU grant PHY-2349677.

APPENDIX

A. The Fermi Velocity of $CoSi_2$

Angle Resolved Photoemission Spectroscopy (ARPES) is a method used to understand the electronic structure of a material. In ARPES, a monochromatic light source is directed at a sample, causing the sample to emit electrons due to the photoelectric effect [12]. By measuring the energy of the ejected electrons along with their emission angle, intensity maps of energy versus emission angle are created. This data is then converted to energy versus momentum spectrum plots.

ARPES can be used to find the fermi velocity, v_F, of a band in a material. The fermi velocity is given by the group velocity of the electrons evaluated at the fermi energy. From classical mechanics

$$v_g = \frac{dw}{dk}. \tag{3}$$

As $E = \hbar\omega$ we find

$$v_g = \frac{1}{\hbar}\frac{dE}{dk}. \tag{4}$$

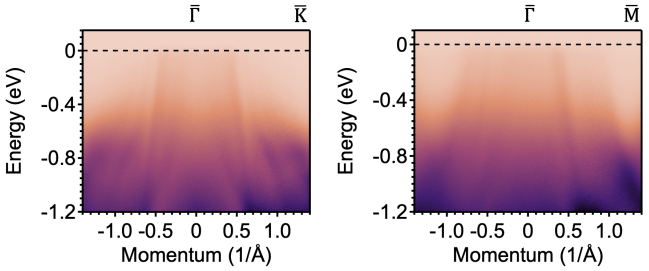

FIG. 8. Momentum spectrum maps for $\overline{\Gamma}$ – $\overline{\mathrm{K}}$ and $\overline{\Gamma}$ – $\overline{\mathrm{M}}$ directions in $CoSi_2$.

By evaluating at the fermi level, we find

$$v_F = \frac{1}{\hbar}\left.\frac{dE}{dk}\right|_{k=k_F}. \tag{5}$$

I used data taken in 2024 at the Advanced Light Source Accelerator to find the fermi velocity of $CoSi_2$. Figure 8 shows the energy versus momentum spectrum graphs for the $\overline{\Gamma}$ – $\overline{\mathrm{K}}$ and $\overline{\Gamma}$ – $\overline{\mathrm{M}}$ directions. The close to vertical lines visible in the spectrum correspond to different bands in the material. For both directions Momentum Distribution Curves (MDCs) were used to find the fermi velocity. An MDC is created by integrating over a narrow energy range at all possible k values to create a curve representing intensity as a function of momentum. MDCs are then created for multiple energy values. An example MDC is shown in Figure 9. MDCs were created for the $\overline{\Gamma}$ – $\overline{\mathrm{K}}$ and $\overline{\Gamma}$ – $\overline{\mathrm{M}}$ directions. The peak positions of the MDCs curves represent different energy bands. MDCs were fit using a linear combination of voigt functions in order to precisely determine the peak locations corresponding to each band. The energy corresponding to each MDC is also known, allowing us to calculate the fermi velocity by Equation 5. MDCs along with the peak positioning and corresponding curve fits for each band are shown in Figure 10. Values for each band are computed via Equation 5 and given in Table I.

TABLE I. Fermi velocity (v_F) in $CoSi_2$ - using uncertainties

Band	v_F for $\overline{\Gamma}$ – $\overline{\mathrm{K}}$ (m/s)	v_F for $\overline{\Gamma}$ – $\overline{\mathrm{M}}$ (m/s)
A	(1.4 ± 0.2) e+06	(8.7 ± 0.1) e+05
A′	(-1.3 ± 0.4) e+06	(-7.7 ± 0.3) e+05
B	(9.7 ± 0.3) e+05	
B′	(-8.3 ± 0.2) e+05	
C	(6.2 ± 0.2) e+05	(7.4 ± 0.6) e+05
C′	(-5.5 ± 0.3) e+05	
D	(5.0 ± 0.4) e+05	(4.7 ± 0.2) e+05
D′	(4.7 ± 0.3) e+05	

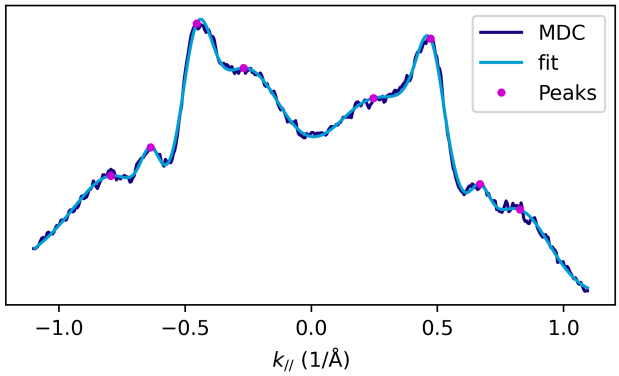

FIG. 9. An example MDC and curve fit along with the peak locations corresponding to each voigt function.

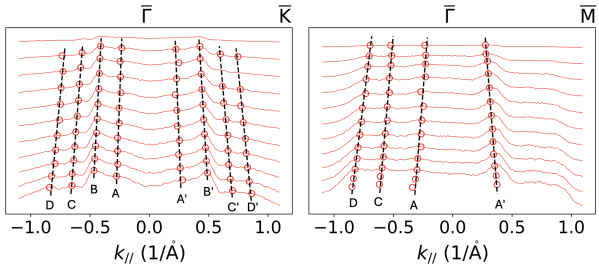

FIG. 10. Momentum Distribution Curves (MDCs) for $\overline{\Gamma}$ – $\overline{\mathrm{K}}$ and $\overline{\Gamma}$ – $\overline{\mathrm{M}}$ directions. MDCs are integrated over 0.04 eV windows. Circles in red shown peak locations along the MDCs while the black dashed lines show a linear curves of best fit. Labels A, B, C, and D designate distinct bands.

B. Table of Measured Samples

Table II shows data for samples used in this paper. The Arsenic and Antimony flux for each sample layer, along with the predicted Arsenic fraction and corresponding lattice constant are shown. All samples except samples YW104, YW105, YW120-123 were grown directly on GaSb. Samples YW104, YW105, YW120-123 were grown on an InAsSb layer which was grown on top of the GaSb (100) substrate.

[1] A. Das, P. Acharyya, S. Das, and K. Biswas, High thermoelectric performance in entropy-driven $Ge_{1-2x-y}Pb_xSn_xSb_yTe$, J. Mater. Chem. A **11**, 12793 (2023).

[2] G. J. Snyder, Thermoelectric energy harvesting, in *Energy Harvesting Technologies*, edited by S. Priya and D. J. Inman (Springer US, Boston, MA, 2009) pp. 325–336.

[3] C. Oses, T. Li, X. Xu, G. Han, G. Qiu, and J. R. Owens, Beyond the four core effects: revisiting thermoelectrics with a high-entropy design, Mater. Horiz. , (2025).

[4] R. Magri, A. Zunger, and H. Kroemer, Evolution of the band-gap and band-edge energies of the lattice-matched gainassb/gasb and gainassb/inas alloys as a function of composition, Journal of Applied Physics **98**, 043701 (2005), https://pubs.aip.org/aip/jap/article-pdf/doi/10.1063/1.2010621/14956618/043701_1_online.pdf.

[5] C. Downs and T. Vandervelde, Progress in infrared photodetectors since 2000, Sensors **13**, 5054 (2013).

[6] C. Kittel, *Introduction to Solid State Physics*, 8th ed. (John Wiley & Sons, New York, 2004) Chap. Chapter 8: Semiconductor Crystals.

[7] U. Mishra and J. Singh, *Semiconductor Device Physics and Design*, 1st ed. (Springer Publishing Company, Incorporated, 2007).

[8] V. Sorokin, S. Sorokin, A. Semenov, B. Meltser, and S. Ivanov, Novel approach to the calculation of instability regions in gainassb alloys, Journal of Crystal Growth **216**, 97 (2000).

[9] E. K. Müller and J. L. Richards, Miscibility of iii-v semiconductors studied by flash evaporation, Journal of Applied Physics **35**, 1233 (1964).

[10] T. Sabardeil, G. Gregoire, J.-L. Reverchon, V. Trinite, E. Tournié, J.-B. Rodriguez, and A. Evirgen, Mbe growth and properties of gainassb alloys deep inside the miscibility gap, Journal of Crystal Growth **657**, 128107 (2025).

[11] G. F. Harrington and J. Santiso, Back-to-basics tutorial: X-ray diffraction of thin films, Journal of Electroceramics **47**, 141 (2021).

[12] H. Zhang, T. Pincelli, C. Jozwiak, *et al.*, Angle-resolved photoemission spectroscopy, Nature Reviews Methods Primers **2**, 54 (2022).

TABLE II. Experimental Data for Samples Studied

Name	**Temperature (°C)**	**Sb Flux (10^{-7} Torr)**	**As Flux (10^{-7} Torr)**	**As Fraction**	**Lattice Constant (Å)**
YW088	500	300	150	0.229	5.8482
YW088	500	300	50	0.095	6.3557
YW089	500	50	300	0.112	5.8924
YW089	500	100	300	0.199	5.8924
YW089	500	150	300	0.028	5.8924
YW090	500	80	300	0.669	5.8839
YW090	500	100	300	0.605	5.8839
YW090	500	120	300	0.557	5.8839
YW091	470	80	300	0.669	5.9081
YW091	470	100	300	0.605	5.9081
YW091	470	120	300	0.557	5.9081
YW092	500	100	90	0.260	5.7493
YW092	500	100	80	0.248	6.3502
YW092	500	100	75	0.242	6.5106
YW093	500	300	90	0.135	5.7589
YW093	500	300	80	0.128	6.3541
YW093	500	300	75	0.124	6.5147
YW094	500	300	120	0.230	5.7510
YW094	500	300	100	0.199	6.3462
YW095	460	300	110	0.215	5.9692
YW095	460	300	100	0.199	6.0518
YW096	430	300	120	0.230	5.9709
YW096	430	300	110	0.215	6.0358
YW098	420	300	120	0.230	5.9935
YW099	420	300	115	0.223	5.9988
YW099	420	300	110	0.215	6.0464
YW102	430	300	110	0.215	6.0040
YW103	430	300	110	0.215	5.9796
YW104	420	300	105	0.207	6.0058
YW105	500	300	100	0.199	5.9213
YW108	425	300	100	0.199	6.0518
YW108	425	300	105	0.207	6.0040
YW109	430	300	90	0.184	6.0482
YW109	430	300	95	0.192	6.0093
YW110	430	300	80	0.166	6.0340
YW111	470	300	85	0.175	6.2599
YW111	470	300	95	0.192	5.8378
YW112	430	300	65	0.140	6.0518
YW112	430	300	55	0.122	6.1169
YW113	430	300	50	0.112	5.8297
YW113	430	300	45	0.103	6.1408
YW113	430	300	40	0.088	6.3342
YW114	430	300	63	0.136	5.7907
YW114	430	300	62	0.134	5.9212
YW114	430	300	61	0.132	6.3364
YW115	470	300	89	0.182	6.3865
YW115	470	300	91	0.185	5.9095
YW116	430	300	59	0.129	5.5508
YW116	430	300	58	0.127	5.9400
YW116	430	300	57	0.125	6.3224
YW117	425	300	55	0.122	6.3204
YW117	425	300	58	0.127	5.9297
YW117	425	300	60	0.131	5.7907
YW119	420	300	55	0.122	6.3523
YW119	420	300	60	0.131	5.9331
YW120	420	300	58	0.127	5.7164
YW121	425	300	58	0.127	5.7132
YW122	440	300	58	0.127	5.6978
YW123	470	300	58	0.127	5.7055